*Research Article*

# Mechanical Investigation of Carbon Steel under Strong Corrosion Effected by Corrosion Pits

**Fan Yang ⬤,[1] Miao M. Yuan,[2] Wen J. Qiao,[1] Na N. Li,[3] and Bin Du[1]**

[1]*Civil and Architecture Engineering, Xi'an Technological University, Xi'an 710021, China*
[2]*School of Civil Engineering, Inner Mongolia University of Science and Technology, Baotou 014010, China*
[3]*School of Civil and Traffic Engineering, Shanghai Urban Construction Vocational College, Shanghai 200438, China*

Correspondence should be addressed to Fan Yang; yangfan0314@xatu.edu.cn

This study investigated the effect of corrosion pits on the mechanical degradation of steel Q345 under strong acid corrosion. The experiment on a total of 27 steel Q345 specimens corroded by 36% industrial hydrochloric acid for 0 h, 1 h, 2 h, 4 h, 8 h, 12 h, 24 h, 48 h, and 72 h, respectively, is conducted to study failure mode and stress-strain curves. After that, a noncontact topography scanner (DSX500) scanned geometric parameters of corrosion pits in steel Q345 to establish its mechanical degradation. The surface morphology and the corresponding degradation law of corroded steel are also revealed. In addition, the steel plastic fracture criterion taking into account equivalent plastic fracture strain and average stress triaxiality $T$ is adopted to propose the uniform pit model. The analysis results show that the failure mode gradually changes from ductile to brittle. It is noted that the depth and relative size of the corrosion pit are the main factors affecting the increase of the maximum pit coefficient. Further, FEM based on uniform corrosion pits is found by the flexible damage evolution criterion. Its calculation results are entirely consistent with experimental results, indicating that this model can mirror the surface morphology of steel suffering strong corrosion, and simulated accurately stress flow law and necking failure of strong corrosion steel. The proposed criterion is validated with verification results and can provide good references for the design of steel bridges under strong corrosion.

## 1. Introduction

The cumulative damage, suffering from corrosion, can significantly reduce the mechanical performance of steel bridges during their entire life. Note that the number of tank trucks loaded with hazardous chemicals increases. When the transport vehicle carrying corrosive liquid overturns, the leakage of strong corrosive liquid will cause strong corrosion behavior on the steel bridge. In the past 10 years, there have been about 284,000 hydrochloric acid leakage accidents in China, threatening the operational safety of bridges [1]. Because strong acid will quickly form corrosion pits in steel, and more plastic strain will accumulate around corrosion pits, those pits cause stress concentration and irreversible mechanical degradation of steel in a short time [2]. Therefore, it is urgent to evaluate

the reduction in load-bearing capacity of components in structures so as to assess the safety of in-service steel bridges, which can contribute to research the law of mechanical degradation of steel after strong corrosion, and make out rescue plans for in-service steel bridges exposed to strong corrosion. The above studies can represent the essential theoretical significance and engineering application value.

As the fact became known, corrosion can cause strength and ductility degradation of steel [3, 4], premature fracture [5], microcracks [6], and degradation of structural seismic performance [7, 8]. In practice engineering, it is a meaningful task to appraise the mechanical properties of steel caused by corrosion pits. It can further determine an effective reinforcement way considering safety, rational design, and technical economy.

At present, numerous studies have been done on the surface morphology of corroded steel, the growth pattern, and the mechanical properties of corrosion pits in China and abroad. These proposed methods that assessed corrosion degree include 3D optics, CT scanning, and weight loss measurement [9]. The degradation law of mechanical properties of corroded steel was acquired by data from surface morphology [10]. From flat and angular specimens with cross-section loss rate of 0–0.384 by tests, the stress-strain curve was also obtained. Moreover, an established method calculated the minimum cross-sectional area of flat and angular specimens [11]. The eddy current method calculated corrosion morphology in theory, which was in good agreement with the model of laser displacement meter in practice [12]. The finite element model analyzed mechanical properties affected by corrosion pits by importing the actual corrosion surface data into Geomagic Studio software [13].

To study the mechanism and growth of pits, research of Chinese and foreign scholars provided a specific basis for evaluating the mechanical properties of pits [14]. Monte Carlo simulation was used to study the probability dispersion of depth and growth rate of corrosion pits in underground pipelines [15]. According to the above study, pit sizes (a or c) and the spatial distance (S) between the presence of critical pits and adjacent critical pits have a significant impact on the mechanical properties of corroded steel [16]. Furthermore, there was a strong stress field inside the pitting degradation model. The stress intensity factor (SIF) value was also more extensive, which was affected by ratios of the pit depth to radius along thickness direction [17, 18]. In addition, the J-integral method simulated the three-dimensional state near the crack to determine the K evolution curve along the thickness direction [19]. It was worth that the concentration and temperature of NaCl solutions also interfere with the development of pitting corrosion. This research had also pointed out that pits increased in diameter and depth in the initial stage and only increased along with depth in the later stage [20]. Meanwhile, the formation of pits, such as the shape, size, and dispersion, was random, so corrosion pits in steel could be described as a random field [21]. From this study, it can be clear that the larger the aspect ratio of the corrosion pit, the more pronounced reduction in bearing capacity. Therefore, these corrosion pits were the most dangerous [22, 23]. Due to the irregularity and randomness of pits in corroded steel, FEM was very complicated based on pits in practice. Therefore, it is necessary to establish a simplified model to simulate pits in practice.

To sum up, although many studies have been conducted on steel specimens under atmospheric corrosion, few of them focused on steel corroded by strong acid. In particular, the effect of corrosion pits on the mechanical degradation of steel Q345 under strong corrosion was still unclear. In this study, the relationship between the characterization parameters of corrosion pits and the mechanical degradation of bridge steel is founded through surface morphology scanning and tensile test for steel Q345 corroded by 36% industrial hydrochloric acid. A simplified uniform pit model is established based on the steel plastic fracture criterion of equivalent plastic fracture strain and average stress triaxiality T. The proposed model lays a foundation for mechanical performance analysis of steel structures after strong acid corrosion and provides a postdisaster damage assessment.

## 2. Experimental Introduction

*2.1. Design of Specimen.* The specimens, made of low-carbon Q345 steel, were purchased in Qinhuangdao Steel Co., Ltd. and taken from 1/4 width of steel by a full-thickness manner (8 mm). The materials conformed to the requirements of Steel and Steel Products - Location and Preparation of Test Pieces for Mechanical Testing (GB/T 2975, 1998) [24]. Meanwhile, the chemical composition of steel also met the standard requirements of High Strength Low Alloy Structural Steels (GB/T 1591, 2008) [25], as listed in Table 1.

The detailed dimensions of specimens in Figure 1 were presented per Metallic Materials - Tensile Testing - Part 1: Method of Test at Room Temperature (GB/T 228.1, 2010) [26].

*2.2. Experiment Program.* In order to simulate bridge steels suffering strong corrosion by industrial acid, specimens with three per group were placed in a glass container, and then 36% industrial hydrochloric acid was added into a container to soak specimens. The whole process of the test can be divided into the following phase: first, these numbered specimens were weighed by an electronic balance (accurate to 0.01 g) so as to record the mass of each specimen before corrosion. Second, 24 standard specimens were immersed into 36% hydrochloric acid solution at room temperature (Figure 2). After corrosion, the specimens were neutralized with 3% sodium carbonate solution to clean corrosion products on the steel surface, when taken out, and then dried by a dryer. Finally, the corroded specimens were weighed by an electronic balance again to record the mass of each specimen after corrosion. Moreover, the residual concentrations of hydrochloric acid after soaking for 1 h, 2 h, 4 h, 8 h, 12 h, 24 h, 48 h, and 72 h were 35%, 29%, 28%, 27%, 27%, 25%, 24%, and 23%, respectively. It can be found from the above data that the residual concentration of hydrochloric acid gradually decreased from 35% in 1 h to 23% in 72 h.

The tensile test was conducted by an electronic universal testing machine (DNS200) with a maximum value of 200 kN and an accuracy class of 0.5. Specific steps were recommended by Metallic Materials - Tensile Testing - Part 1: Method of Test at Room Temperature (GB/T 228.1, 2010) [26]. The tensile test was carried out by displacement control and specially set up an extensometer of 50 mm length. The loading rates at the elastic, yield, and strengthening stages were 0.75 mm/min, 0.75 mm/min, and 5.0 mm/min, respectively.

## 3. Experimental Results

*3.1. Surface Morphology Characteristics.* The DSX500 non-contact surface morphology instrument was adopted to measure the surface morphology of corrosion steel after removing corrosion products (Figure 3). The scanning area

TABLE 1: Chemical compositions of Q345 (wt.%).

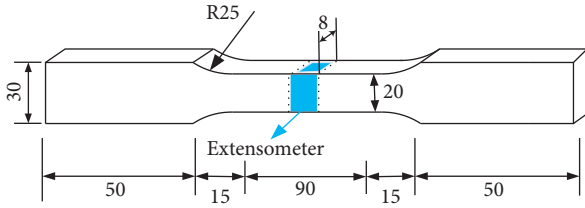| C | Si | Mn | P | S | Al | Fe |
|------|------|------|------|------|------|------|
| 0.16 | 0.25 | 1.25 | 0.02 | 0.02 | 0.01 | Bal. |



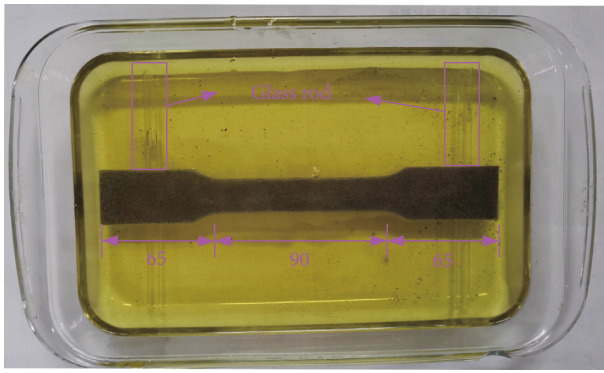FIGURE 1: Dimensions of test specimen (mm).
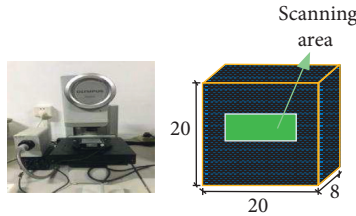


FIGURE 2: Corrosion of test specimen.



FIGURE 3: Scanned area (mm) and 3D noncontact surface morphology instrument (DSX500).

in the centroid of the corroded steel was $40 \, \text{mm} \times 20 \, \text{mm}$. The morphology and pitting corrosion data of corroded steel can be obtained under vertical and horizontal scanning steps of $50 \, \mu\text{m}$.

Figures 4 and 5 show the three-dimensional surface morphology of steel Q345 after strong corrosion by hydrochloric acid under different corrosion times [27]. It can be found that forms of pits in steel after the corrosion of hydrochloric acid can be divided into uniform pinhole, cone, and ellipsoid shapes.

As shown in Figures 4 and 5, at the initial stage of corrosion, due to the high chloride ion concentration in 36% hydrochloric acid solution, the surface morphology of steel is uniform. When the corrosion time increases, the pit depth increases unevenly and spreads along the width of steel too. Table 2 lists the parameters of the corrosion pits.

As listed in Table 2, when the corrosion time reaches 1 h, $\Delta d_{ave}$ and $\omega_{ave}$ of steel Q345 are 27.607 $\mu$m and 102.755 $\mu$m, respectively. Pits are scattered and mainly in pinhole shape. When the corrosion time is 12 h, $\Delta d_{ave}$ and $\omega_{ave}$ of steel Q345 are 68.037 $\mu$m and 187.518 $\mu$m, respectively. The width and depth of pits increase gradually, and the number of pits increases slowly. Meanwhile, pits are mainly in the shapes of saddle and cone. When the corrosion time reaches 72 h, $\Delta d_{ave}$ and $\omega_{ave}$ of steel Q345 are 97.044 $\mu$m and 327.166 $\mu$m, respectively. It can be found from the above data that the number of pits increases slowly, and the width and depth further increase. The adjacent pits on the steel surface merge into large local pits with the shape of ellipsoid and hemisphere.

Figure 6 shows a fitting curve of the maximum depth and corrosion times aimed at the corrosion pit. The maximum width of corrosion pits is fitted to corrosion times, as illustrated in Figure 7. It can be inferred from Figures 6 and 7 that the pit depth and pit width of steel Q345 increase nonlinearly with the corrosion time. The change law is shown in equations (1) and (2).

At the beginning of corrosion, the depth and width of corrosion pits increase very quickly. When the corrosion time reaches 10 h, the size of corrosion pits in steel Q345 grows slowly. This change is because the decrease of chloride ion concentration and production of ferric chloride hinder the reaction rate:

$$\Delta d_{\text{ave}} = 88.01 - 69.99 \exp\left(\frac{-x}{9.55}\right) R^2 = 0.96, \tag{1}$$

$$\omega_{\text{ave}} = 344.15 - 241.43 \exp\left(\frac{-x}{37.66}\right) R^2 = 0.95. \tag{2}$$

In order to intuitively reflect the changing law of pits morphology with the increase of corrosion times, three-dimensional roughness parameters of steel Q345 (Table 3) were defined as geometric characteristics of surface morphology of the specimen by three-dimensional scanning.

$\rho_{ave}$ is the average corrosion rate, $S_a$ is the arithmetic mean height of height: $S_a = 1/A \int \int Z(x, y) \, dx \, dy = 1/MN \sum_{i=1}^{M} \sum_{j=1}^{N} |Z(x_i, y_j)|$, $S_q$ is the root-mean-square deviation of height: $S_q = \sqrt{1/A \int \int z^2(x, y) dx \, dy}$, $S_p$ is the maximum peak height: $S_p = \max Z(x, y) = \max Z(x_i, y_j)$, $S_v$ is the maximum depth of valley bottom: $S_v = |\min Z(x, y)| = |\max Z(x_i, y_j)|$, $S_z$ is the maximum surface height $S_z = S_p + S_v$, $Z$ is the fitted intermediate plane by the least-square distance method based on actual corrosion plane.

In the mid-plane of the corroded steel, $S_a$ and $S_q$ are parameters to judge deviation of surface morphology. The relationship between $S_a$ and corrosion times is obtained by fitting, as shown in Figure 8. $S_q$ correlated and corrosion times are also fitted in Figure 9.

It can be observed from Figures 8 and 9 that three-dimensional roughness parameters of steel Q345 increase nonlinearly with corrosion times. Once corrosion time exceeds 10 h, the slope of curves in these figures significantly slows down. The relationship between $S_a$ and corrosion
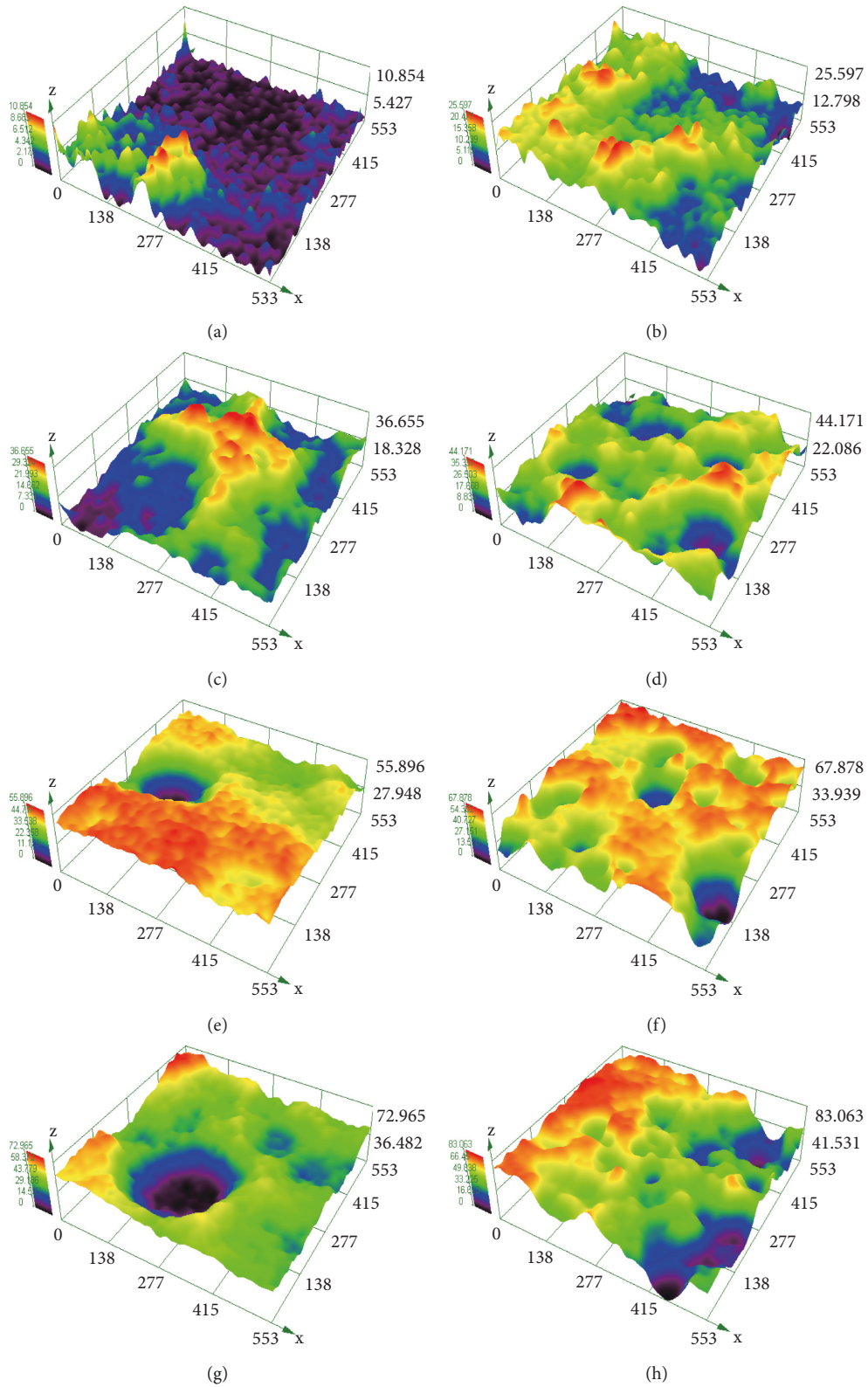
(a)



(b)



(c)



(d)



(e)



(f)
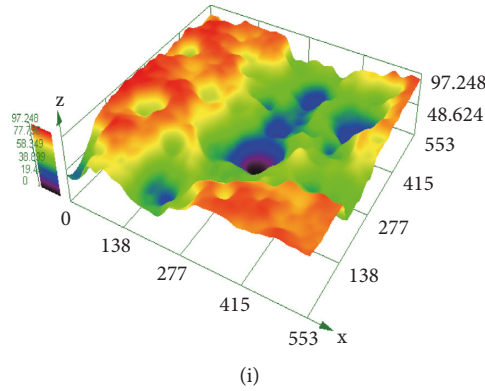


(g)



(h)

FIGURE 4: Continued.

(i)

FIGURE 4: Three-dimensional scanning data of corrosion test piece ($\mu$m). (a) 0 h, (b) 1 h, (c) 2 h, (d) 4 h, (e) 8 h, (f) 12 h, (g) 24 h, (h) 48 h, and (i) 72 h.

times of steel is shown in equation (3). Equation (4) fits the relationship between $S_q$ and corrosion times of steel:

$$S_a = 2.769 + 17.057x^{0.339} \quad R^2 = 0.96, \tag{3}$$

$$S_q = 3.555 + 15.859x^{0.357} \quad R^2 = 0.98. \tag{4}$$

*3.2. Destruction Form.* The damage morphology of corroded steel can be determined according to its fracture morphology [27–29], including three different fracture morphologies. With the prolongation of corrosion times, the stress concentration caused by corrosion pits contributes to irregular fracture paths and gradually increases roughness. The morphology of the fracture area is also related to strong corrosion surface morphology; after comparing three fracture morphologies, the deformation details are zoomed in in Figure 10.

An electron microscope, taking the magnification of 3000 times, was used to observe the microscopic morphology of fracture in steel under different corrosion times (Figure 11). The scanning position is near the central area of the fracture. It can be seen from Figure 11 that the microscopic fracture morphology of the specimen mainly shows up as shallow dimples accompanied by micropores with the extension of corrosion time. At the initial stage of corrosion time of 1–24 h, tiny bubbles were observed on the surface of the specimen; that is, there was a hydrogen evolution reaction in this process. Nevertheless, Figure 11(a) exhibits that the dimples of the microscopic fracture morphology were larger, which was obviously a ductile fracture. While the fracture of hydrogen embrittlement was an intergranular fracture, indicating that the corrosion pit exerted a considerable impact on the fracture. As the corrosion time elapses, the number of dimples gradually increases, and their size gradually decreases. Moreover, the microfracture mechanism of the corroded steel changes from micropore nucleation to dissociation and fracture. As a result, the state of the fracture model changes from ductile damage to brittle damage.

*3.3. Tensile Test Results.* There were 3 specimens per group with the same corrosion condition. Table 4 lists the mechanical index values of specimens under a specific corrosion time, including elastic modulus $E_s$, nominal yield strength $f_y$, nominal ultimate strength $f_u$, yield strength ratio $f_y/f_u$, and elongation $\delta_s$.

In addition, the elongation of corrosion steel is lower than that of uncorroded specimen at the same strain rate during the tensile test; that is, the corroded specimen is sensitive to stress corrosion. Overall, the smaller the relative value of elongation is, the more sensitive the stress corrosion is. Hence, such loss coefficient of elongation is taken as a stress sensitivity index, and then equation (5) elucidates stress corrosion sensitivity [29]:

$$I(\delta) = \left(1 - \frac{\delta_s}{\delta_{s0}}\right) \times 100\%, \tag{5}$$

where $\delta_s$ is the elongation of corroded specimens, $\delta_{s0}$ is the elongation of uncorroded specimens, and $I(\delta)$ is stress corrosion sensitivity.

It can be concluded from Table 4 that elastic modulus, nominal yield strength, nominal ultimate strength, and elongation decrease accordingly over the corrosion time. First, when the stress corrosion sensitivity is 6.31%, 12.25%, 18.42%, 23.93%, 27.92%, 32.35, 36.98%, and 42.18%, respectively, the elastic modulus of steel fell by 2.01%, 4.24%, 7.65%, 10.15%, 12.17%, 14.74%, 15.70%, and 19.86%, respectively. Second, the nominal yield strengths decrease by 2.63%, 4.10%, 5.53%, 6.64%, 7.59%, 8.21%, 9.10%, and 10.96%, respectively. Third, the nominal ultimate strengths decrease by 0.94%, 2.19%, 2.99%, 3.66%, 4.53%, 5.22%, 6.19%, and 7.20%, respectively. Evidently, the nominal yield strength and the nominal ultimate strength of the corrosion steel represent a slower downward trend, while the elastic modulus shows a faster downward trend. In addition, it can be concluded from Table 4 that with the increase of corrosion time, gradually, the dip in elongation of all specimens is smaller than uncorroded specimens, showing stress corrosion sensitivity.
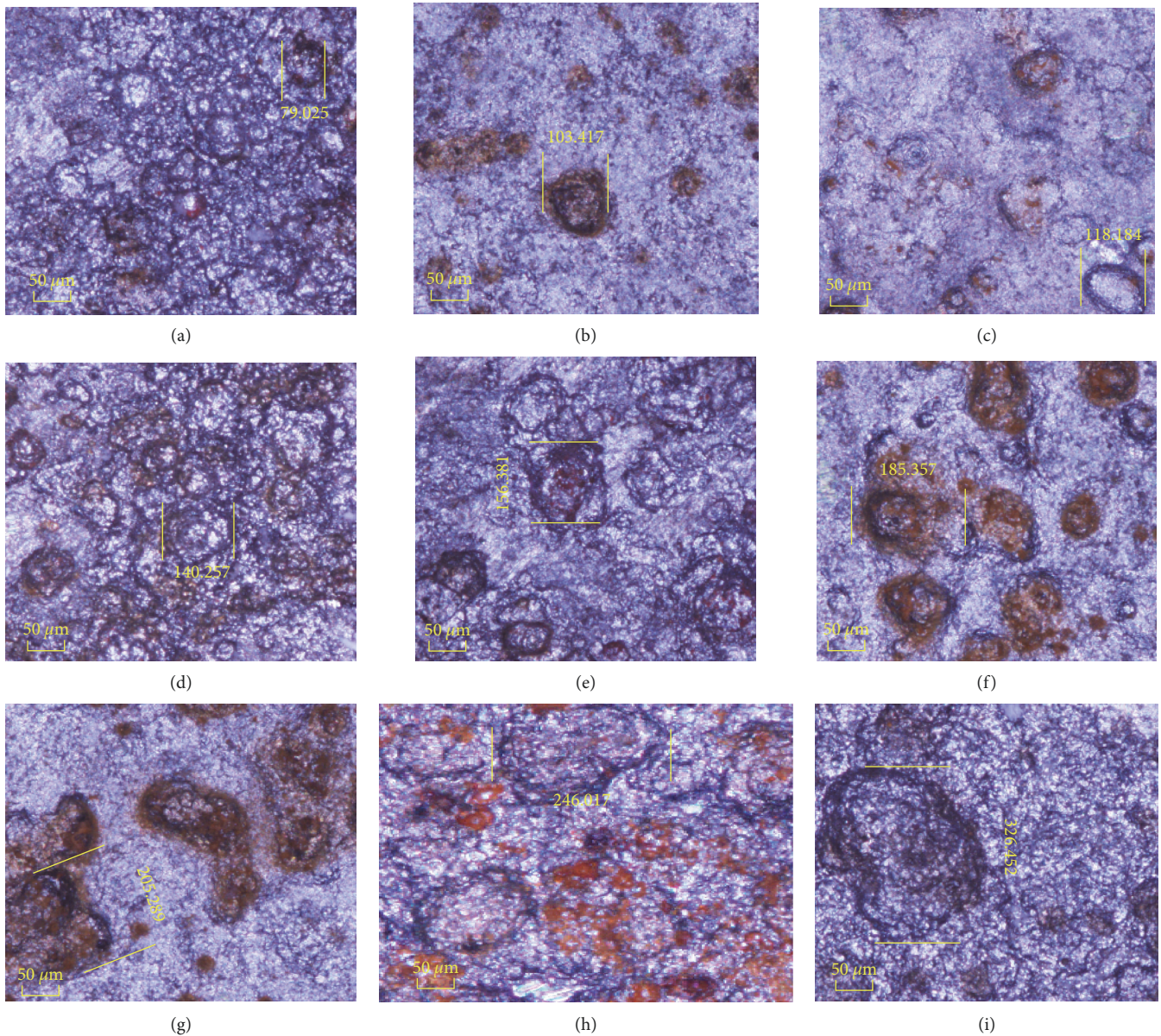
FIGURE 5: Three-dimensional diagram of corrosion test piece. (a) 0 h, (b) 1 h, (c) 2 h, (d) 4 h, (e) 8 h, (f) 12 h, (g) 24 h, (h) 48 h, and (i) 72 h.

TABLE 2: The parameters of the corrosion pits.

| Corrosion time (h) | 0 | 1 | 2 | 4 | 8 | 12 | 24 | 48 | 72 |
|---|---|---|---|---|---|---|---|---|---|
| $\Delta d_{ave}$ ($\mu m$) | 10.742 | 27.607 | 35.870 | 44.850 | 57.589 | 68.037 | 74.020 | 84.060 | 97.044 |
| $\omega_{ave}$ ($\mu m$) | 78.980 | 102.755 | 119.650 | 140.752 | 159.833 | 187.518 | 209.490 | 247.053 | 327.166 |

$d_{ave}$ is the average value of the maximum pit depth and $\omega_{ave}$ is the average value of the maximum pit width.

### 3.4. Relationship between Influence Coefficient of Maximum Corrosion Pit and Mechanical Properties.

From previous research, the mechanical degradation of the model about the corroded steel is related to the three-dimensional measurement of the corrosion pit and thickness of the specimen, which can be analyzed by the corrosion pit schematic diagram (Figure 12).

The width and depth of the largest pit increase over the corrosion time, but the thickness of specimens decreases. It also can be found from Figure 12 that the effect of the same depth and width of pit on different thicknesses of steel can bring out different stress concentrations. Therefore, $\Delta d/\omega$ (ratio of depth to width of the largest pit) and $\Delta d/h$ (ratio of the depth of the largest pit to the thickness of specimens) are considered the maximum pit impact factor, which can comprehensively express the influence of three-dimensional on mechanical degradation after corrosion. The equation is as follows:
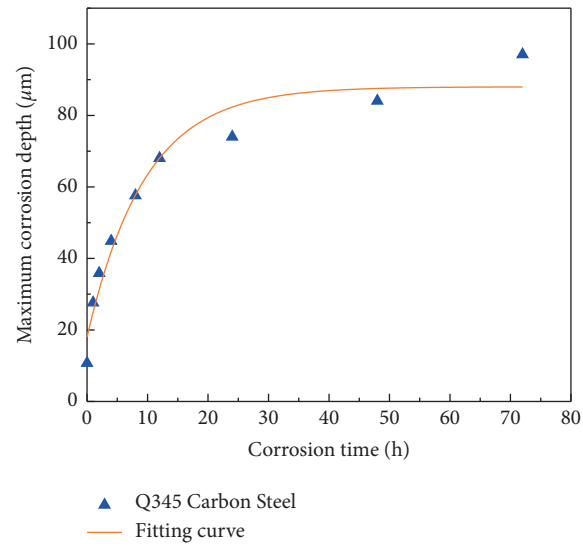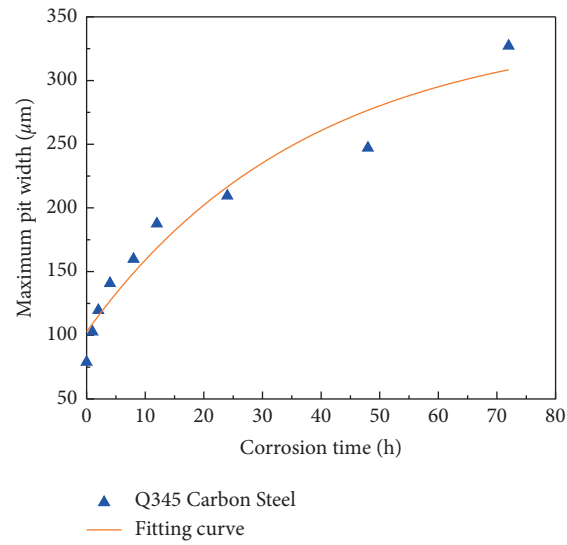
FIGURE 6: Relationship between corrosion time and $\Delta d_{ave}$.



FIGURE 7: Relationship between corrosion time and $\omega_{ave}$.

TABLE 3: Three-dimensional roughness parameters of steel Q345.

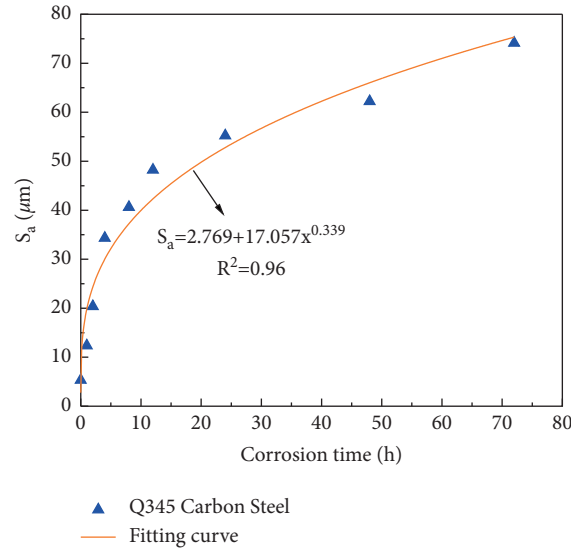| Corrosion time (h) | $S_a$ | $S_q$ | $S_p$ | $S_v$ | $S_z$ |
|---|---|---|---|---|---|
| 0 | 5.346 | 6.785 | 36.355 | 45.236 | 78.685 |
| 1 | 12.359 | 13.245 | 58.326 | 72.315 | 123.654 |
| 2 | 20.369 | 22.536 | 85.231 | 96.234 | 150.231 |
| 4 | 34.326 | 34.265 | 101.236 | 120.314 | 224.362 |
| 8 | 40.624 | 38.625 | 114.256 | 138.698 | 242.367 |
| 12 | 48.236 | 46.359 | 119.522 | 159.386 | 285.374 |
| 24 | 55.235 | 52.154 | 128.964 | 169.125 | 308.159 |
| 48 | 62.234 | 66.324 | 135.579 | 182.235 | 335.568 |
| 72 | 74.125 | 76.378 | 151.255 | 204.567 | 405.321 |

FIGURE 8: Relationship between corrosion time and.
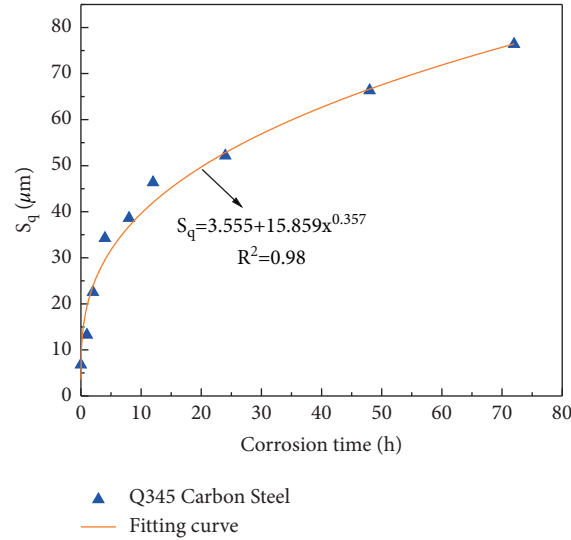


FIGURE 9: Relationship between corrosion time and $S_q$.

$$\zeta_{\max} = \frac{(\Delta\ d)^2}{\omega h}. \tag{6}$$

The degradation relationships between $\zeta_{\max}$ and $E_s$, $f_y$, $f_u$, $f_y/f_u$, $\delta_s$ are fitted (Figure 13) and illustrated by equations (7)–(11):

$$E_s = 215.73 + 22.14\zeta_{\max} - 37.72\zeta_{\max}^2 + 15.81\zeta_{\max}^3 - 2.14\zeta_{\max}^4 R^2 = 0.98, \tag{7}$$

$$f_y = 470.85 - 3.24\zeta_{\max} - 20.21\zeta_{\max}^2 + 10.31\zeta_{\max}^3 - 1.51\zeta_{\max}^4 R^2 = 0.99, \tag{8}$$

$$f_u = 597.29 + 9.63\zeta_{\max} - 26.29\zeta_{\max}^2 + 11.72\zeta_{\max}^3 - 1.64\zeta_{\max}^4 R^2 = 0.99, \tag{9}$$

$$\frac{f_y}{f_u} = 0.782 - 0.007\zeta_{\max} R^2 = 0.99, \tag{10}$$

$$\delta_s = 36.02 + 3.14\zeta_{\max} - 8.82\zeta_{\max}^2 + 3.78\zeta_{\max}^3 - 0.52\zeta_{\max}^4 R^2 = 0.99. \tag{11}$$
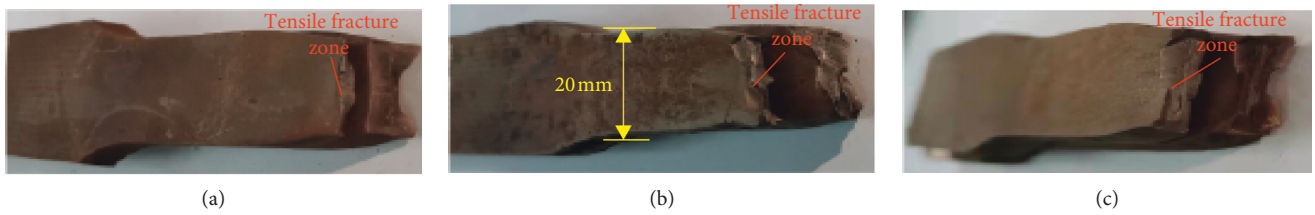
(a)      (b)      (c)

FIGURE 10: Fracture morphology. (a) Arc fracture. (b) Oblique fracture. (c) Ladder fracture.



(a)      (b)      (c)
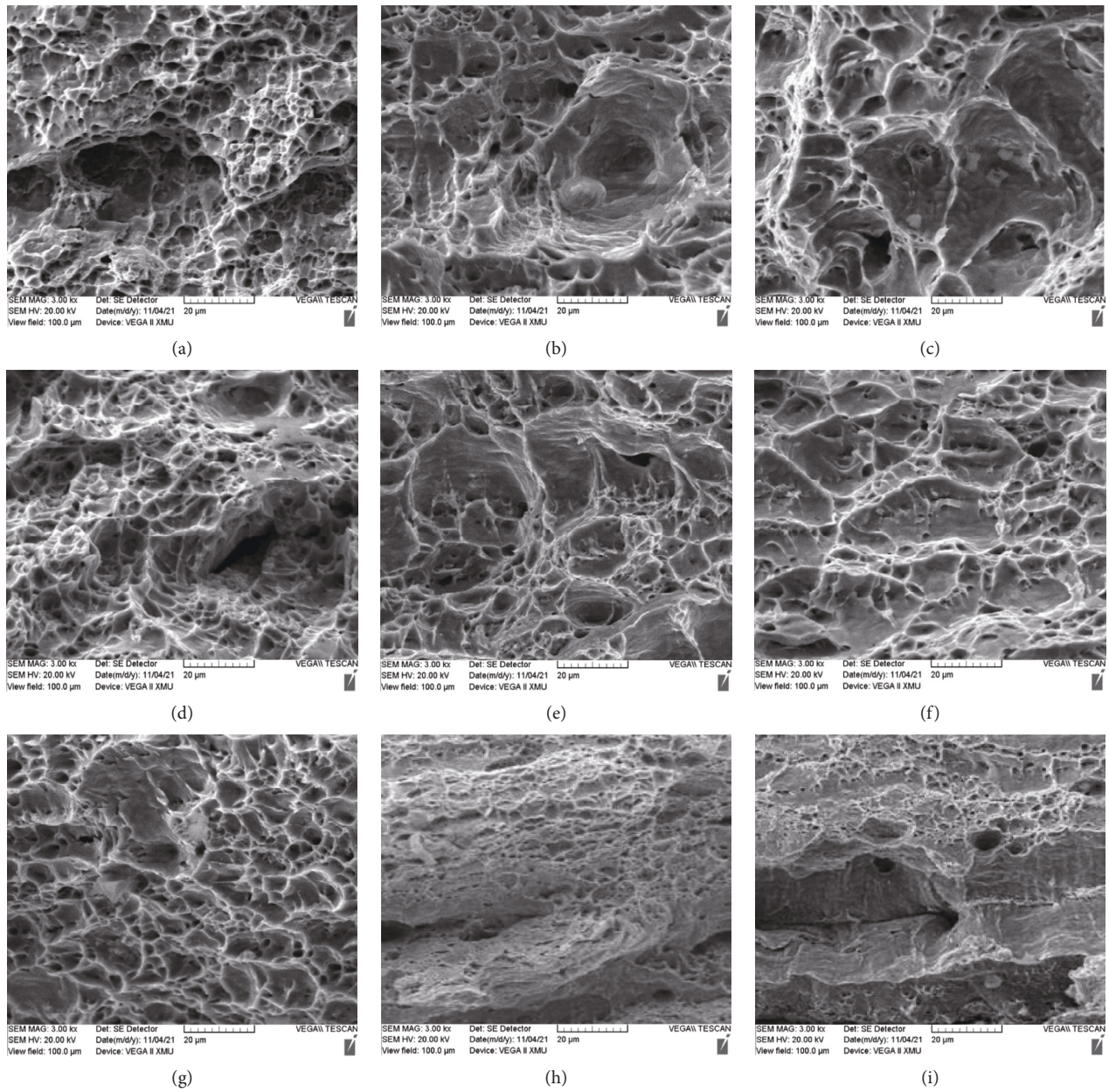
(d)      (e)      (f)

(g)      (h)      (i)

FIGURE 11: Images of corrosion steel fracture. (a) 0 h, (b) 1 h, (c) 2 h, (d) 4 h, (e) 8 h, (f) 12 h, (g) 24 h, (h) 48 h, and (i) 72 h.

TABLE 4: Mechanical properties of strong corrosion steel Q345.

| Corrosion time (h) | $E_s$ (GPa) | $f_y$ (MPa) | $f_u$ (MPa) | $f_y/f_u$ | $\delta_s$ (%) | $I(\delta)$ (%) | $\zeta_{max}/10^{-3}$ |
|---|---|---|---|---|---|---|---|
| 0 | 218.68 | 469.73 | 598.13 | 0.79 | 36.32 | — | 0.18 |
| 1 | 214.29 | 457.38 | 592.50 | 0.77 | 34.03 | 6.31 | 0.92 |
| 2 | 209.60 | 450.46 | 585.02 | 0.77 | 31.87 | 12.25 | 1.35 |
| 4 | 202.65 | 443.75 | 580.25 | 0.76 | 29.63 | 18.42 | 1.81 |
| 8 | 198.10 | 438.52 | 576.26 | 0.76 | 27.63 | 23.93 | 2.64 |
| 12 | 194.57 | 434.10 | 571.03 | 0.76 | 26.18 | 27.92 | 3.16 |
| 24 | 190.01 | 431.17 | 566.91 | 0.76 | 24.57 | 32.35 | 3.36 |
| 48 | 184.34 | 427.01 | 561.11 | 0.76 | 22.89 | 36.98 | 3.69 |
| 72 | 175.25 | 418.25 | 555.09 | 0.75 | 21.00 | 42.18 | 3.77 |
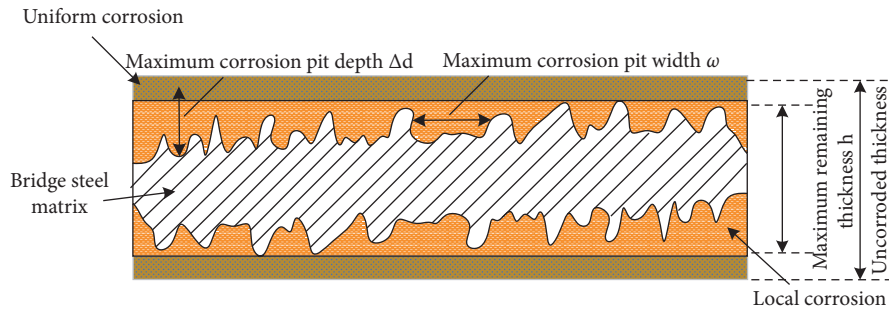


FIGURE 12: Corrosion pit schematic diagram.
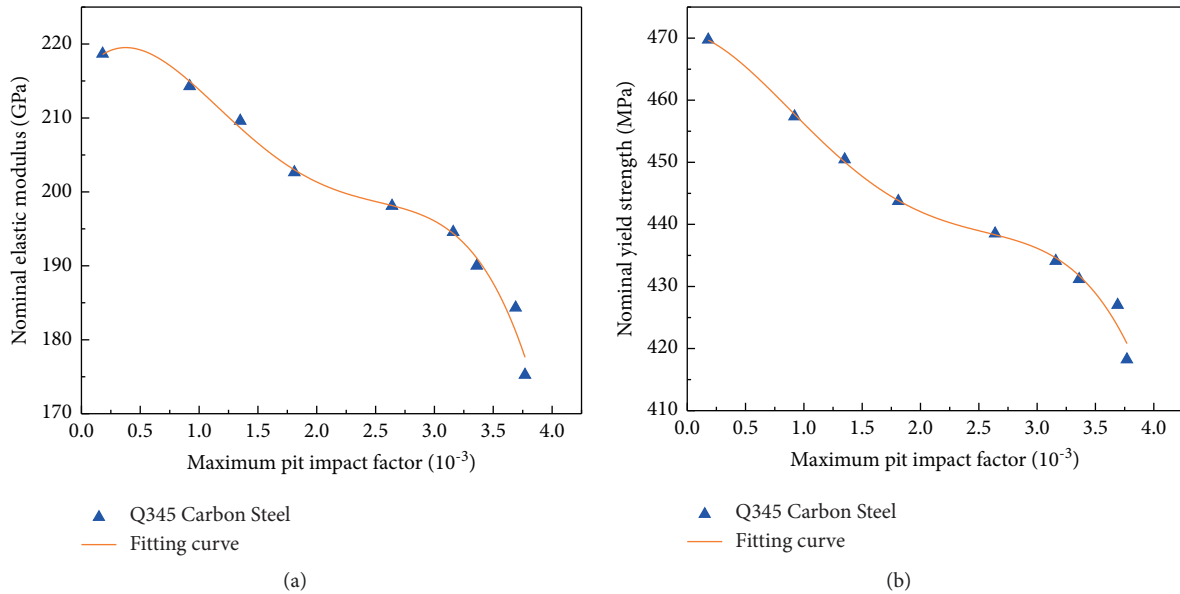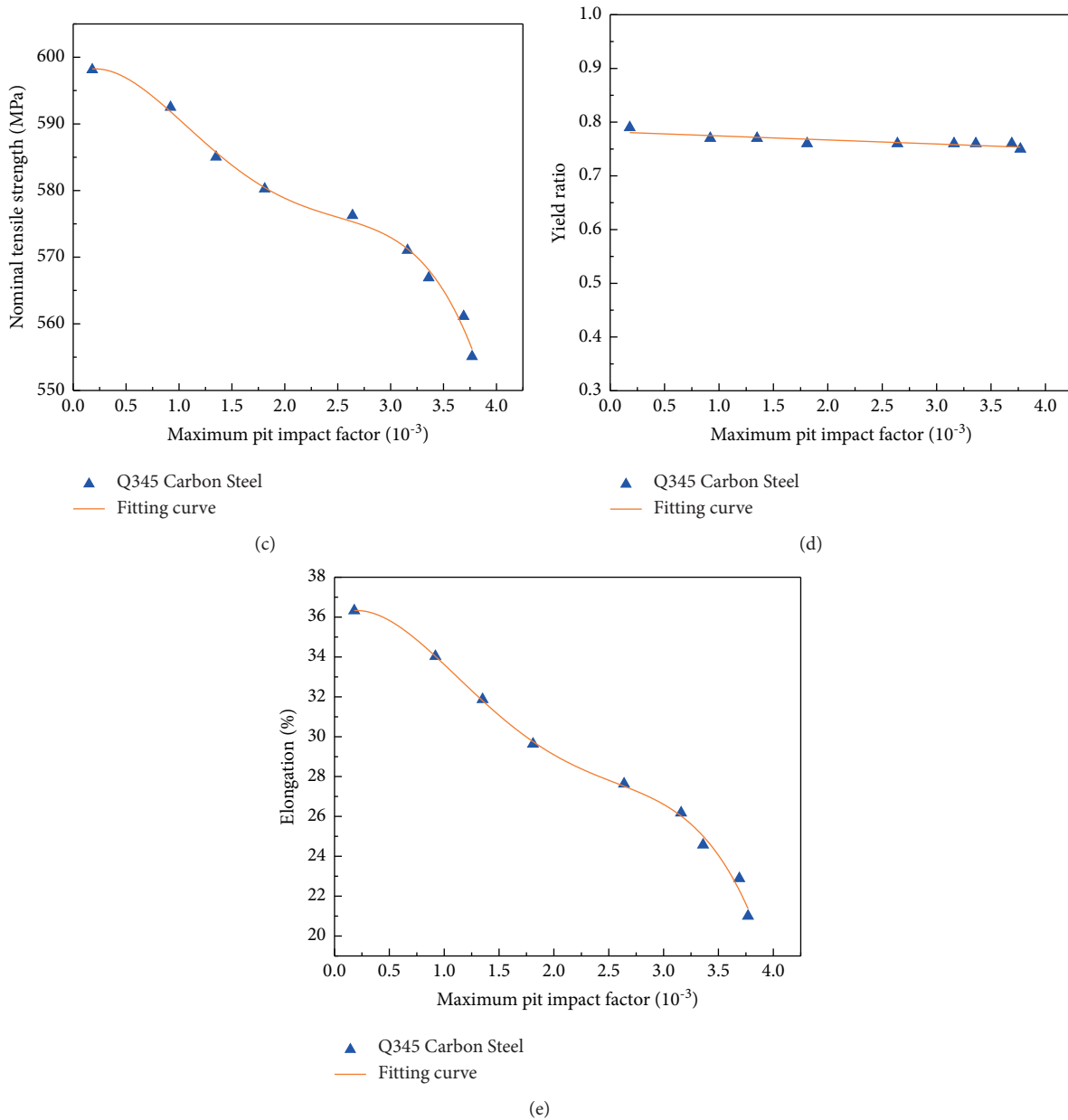


(a)



(b)

FIGURE 13: Continued.

(c)

(d)

(e)

FIGURE 13: Analysis of mechanical degradation properties of the maximum pit impact factor. (a) $\zeta_{max}$ and $E_s$, (b) $\zeta_{max}$ and $f_y$, (c) $\zeta_{max}$ and $f_u$, (d) $\zeta_{max}$ and $f_y/f_u$, and (e) $\zeta_{max}$ and $\delta_s$.

As shown in Figure 13, as the maximum pit impact factor increase with corrosion times, the elastic modulus, nominal yield strength, nominal tensile strength, and elongation of corroded steel represent a gradual decline. The elastic modulus of specimens with corrosion time of 1 h, 2 h, 4 h, 8 h, 12 h, 24 h, 48 h, and 72 h decrease by 1.99%, 4.20%, 7.42%, 9.67%, 10.27%, 12.91%, 15.35%, and 19.55%, respectively. The nominal yield strengths decrease by 3.00%, 4.15%, 5.15%, 6.79%, 7.58%, 8.04%, 9.26%, and 10.37%, respectively; the nominal tensile strengths decrease by 0.69%, 1.55%, 2.59%, 3.35%, 4.02%, 4.71%, 5.54%, and 6.60%, respectively; the elongations decrease by 4.88%, 13.65%, 16.15%, 22.20%, 26.64%, 31.58%, 35.74%, and 41.12%, respectively. When the influence coefficient of the maximum corrosion pits rises, the number and width of corrosion pits of specimens gradually increase, too. Additionally, stress concentration caused by the three-dimensional morphology of pits leads to mechanical degradation of corroded steel. When the maximum pit impact factor is less than $2 \times 10^{-3}$, the mechanical properties of steel Q345 show a linear downward trend; when the former is greater than $2 \times 10^{-3}$, the latter decrease slowly.

## 4. Strong Corrosive Constitutive Model of Steel Q345

The constitutive relation of steel Q345 under strong corrosion is obtained by summarizing the piecewise model in reference [30] as follows:

$$
\sigma = \begin{cases}
E_s \varepsilon & \varepsilon < \varepsilon_y \\[2mm]
f_y & \varepsilon_y \leq \varepsilon \leq K_1 \varepsilon_y \\[2mm]
K_3 f_y + \dfrac{E_s(1 - K_3)}{\varepsilon_y (K_2 - K_1)^2}(\varepsilon - K_2 \varepsilon_y)^2 & \\[4mm]
& K_1 \varepsilon_y \leq \varepsilon \leq K_2 \varepsilon_y
\end{cases}
\tag{12}
$$

where $\sigma$ is the stress, $E_s$ is the elastic modulus, $\varepsilon$ is the strain, $f_y$ is the yield strength, $\varepsilon_y$ is the yield strain, $K_1$ is the ratio of strengthened strain to peak strain, $K_2$ is the ratio of strengthened strain to yield strain, and $K_3$ is the ratio of tensile strength to yield strength, namely, the yield strength ratio. $K_1, K_2, K_3$ are used to control the shape of the constitutive curve.

Figure 14 represents a vital link between $\zeta_{max}$ and $K_1, K_2$. $K_1, K_2$ in steel Q345 change significantly and gradually decrease with the maximum pit impact factor. Thus, $K_1, K_2$ in the degradation model were proposed through regression analysis (equations (12) and (13)). The reason for the decrease is that with further expansion of the corrosion pit, stress concentration becomes more apparent, and the yield platform gradually shortens in steel. As a result, yield strain and initial strain in the strengthening stage decrease slowly. The model parameter K3 that fluctuates within a certain range has no apparent correlation with the maximum pit impact factor. It can be seen that the safety reserve capacity of steel remains unchanged regardless of corrosion times. In order to simplify the model, K3 in the proposed model is a constant suggested to be 1.28 as the minimum value:

$$
K_1 = 12.807 + 1.449x - 0.769x^2 \quad R^2 = 0.87, \tag{13}
$$

$$
K_2 = 122.15 - 2.258x - 2.486x^2 \quad R^2 = 0.87. \tag{14}
$$

## 5. Finite Element Analysis

ABAQUS software established a model according to the size of the specimen in Figure 1, in which mechanical properties of the uncorroded specimen determine material parameters in FEM (mechanical properties are as follows: elastic modulus was $2.2 \times 10^5$ MPa, Poisson's ratio was 0.3, steel density was 7.9 $g/cm^3$, yield strength was 450 MPa, hardening index $n$ was 0.60, and hardening coefficient K was 765 MPa. The loading speed in FEM was the same as that in tests. The loading model was displacement loading, with one end constrained and the other end moved during loading. The unit selecting the C3D8R reduction integral was meshed by hexahedron. FEM set up display dynamics and adopted the automatic incremental step method. The corrosion pit in the FEM rotary cut to simulate that in practice. In FEM, corrosion pits were arranged neatly on one side of the specimen, and the horizontal and longitudinal spacing of corrosion pits were both 2.5 mm, as shown in Figure 15. The true stress-strain curve for material must be used when defining the constitutive relationship of material in FEM, and the engineering stress-strain curve obtained from tests is converted into the true stress-strain curve according to equation (14). Under different corrosion times, the true and nominal stress-strain curves of steel Q345 are shown in Figure 16. The encrypted cell around the corrosion pit was 0.5 mm, and the remaining nonencrypted grid cells were 1 mm, which can attain the calculation accuracy:

$$
\begin{cases}
\sigma_1 = \sigma_0 \times (1 + \varepsilon_0), \\
\varepsilon_1 = \ln(1 + \varepsilon_0).
\end{cases}
\tag{15}
$$

where $\sigma_1$ and $\varepsilon_1$ are the true stress and strain, respectively, and $\sigma_0$ and $\varepsilon_0$ are the nominal stress and strain, respectively.

Figure 16 shows that two stress-strain curves of steel Q345 basically coincide in the elastic and the yield phases. When stress value reaches the ultimate strength, it gradually degrades in the engineering curve but continues to increase in the true curve. Therefore, as strain increases, the gap between true stress and engineering stress becomes increasingly prominent.

The nondamage stage (the stage before reaching the ultimate strength of steel) corresponds to material elasticity and plasticity in ABAQUS. The damage begins when stress comes to its ultimate strength. The process from the beginning of damage to tensile fracture is defined as the damage evolution stage, as shown in Figure 17.

In ABAQUS, material damage and its evolution are set by damage parameters such as flexibility and their corresponding suboptions. The stress triaxiality and equivalent plastic fracture strain are extracted from equation (15) [31]. If the equivalent plasticity reaches the limit state, FEM will delete the plastic element.

The ductile fracture criterion of steel, including equivalent plastic fracture strain $\varepsilon_f^{cr}$ and average stress triaxiality $T$, is shown in equation (15):

$$
\varepsilon_f^{cr} = \frac{C}{3T}, \tag{16}
$$

where C is the criterion parameter of steel ductile fracture $C = \ln(A_0/A)$. Taking into account the nominal stress-strain curve of uncorroded steel, the C in ductile fracture criterion is 1.5 through repeated iterative calculation of FEM parameters; A0 is the original area of steel; A is the area when the steel is broken; $T$ is the stress triaxiality $T \geq 1/3$.

It is noted that the stress triaxiality of each point in the specimen constantly changes during the tensile test. The fracture is caused when the integral of the stress-strain reaches a critical value. Referring to the calculation method in reference [29], the calculation equation of average stress triaxiality $T$ is as follows:
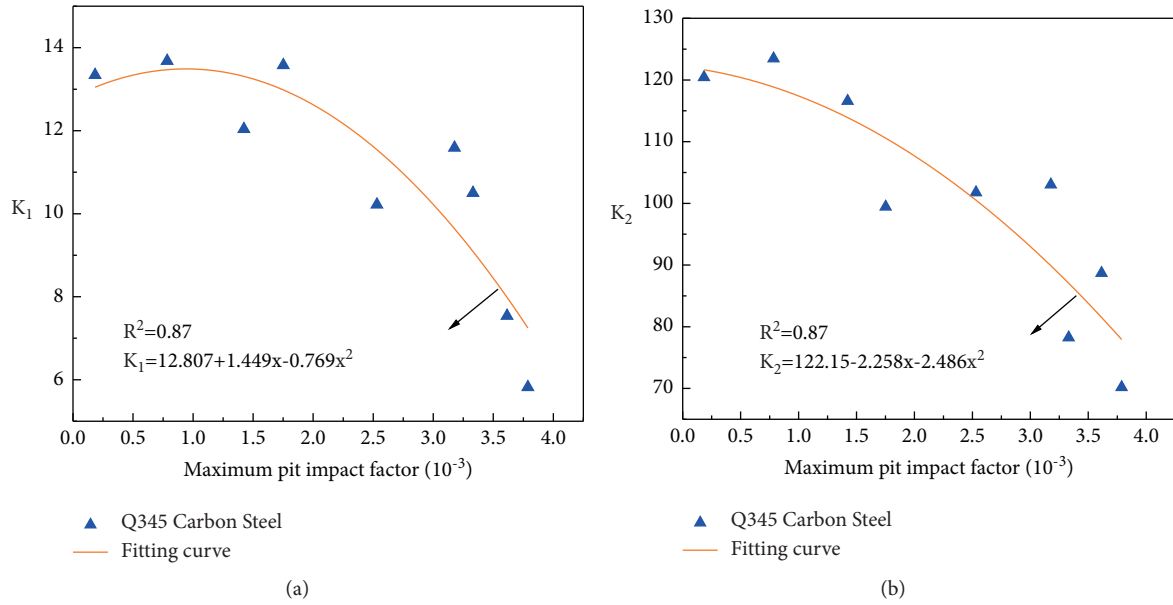
FIGURE 14: The relationship between the maximum pit impact factor $\zeta_{max}$ and $K_1, K_2$. (a) $\zeta_{max}$ and $K_1$ and (b) $\zeta_{max}$ and $K_2$.
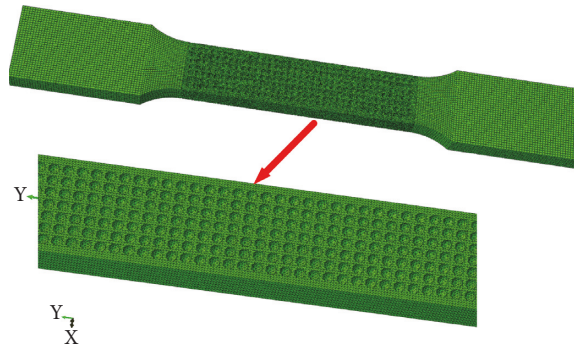


FIGURE 15: Finite element mesh division.

$$T = \frac{\int_0^{\varepsilon_f^{cr}} (\sigma_m/\sigma_e) d\varepsilon^{cr}}{\varepsilon_f^{cr}}, \qquad (17)$$

where $\sigma_m$ is hydrostatic pressure, $\sigma_e$ is Mises equivalent stress, $\sigma_m/\sigma_e$ is stress triaxiality of a point inside steel, and $\varepsilon_f^{cr}$ is equivalent strain of fracture.

It is often difficult to establish a finite element model so as to simulate the corrosion surface in practice. For this reason, a uniform distribution pit model was established in

this study. Based on equation (15), the software adopted the stress-strain curve of strong corrosion steel obtained from the test to develop the FEM under corrosion times of 0 h, 1 h, 2 h, 4 h, 8 h, 12 h, 24 h, 48 h, and 72 h, respectively.

Stress-strain curves of FEM are compared with the test in Figure 18. In the elastic deformation and uniform plastic deformation stages, finite element curves agree well with test curves of corroded steel. However, due to complex stress after necking and only considering the evolution of flexible damage, finite element curves of strong corrosion steel have
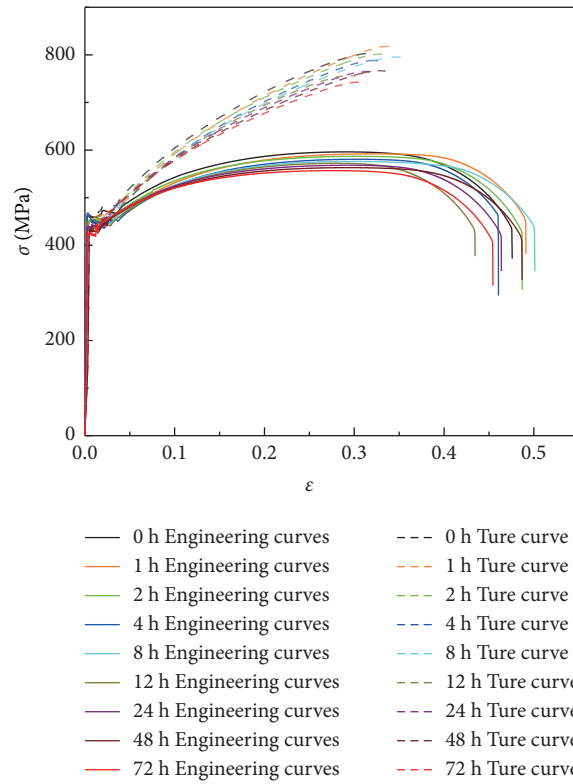
FIGURE 16: True stress-strain curve and nominal stress-strain curve of steel Q345 with different corrosion times.
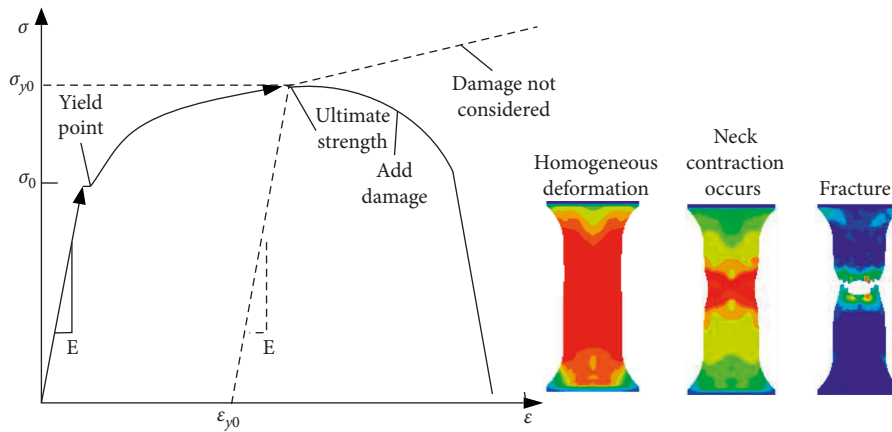


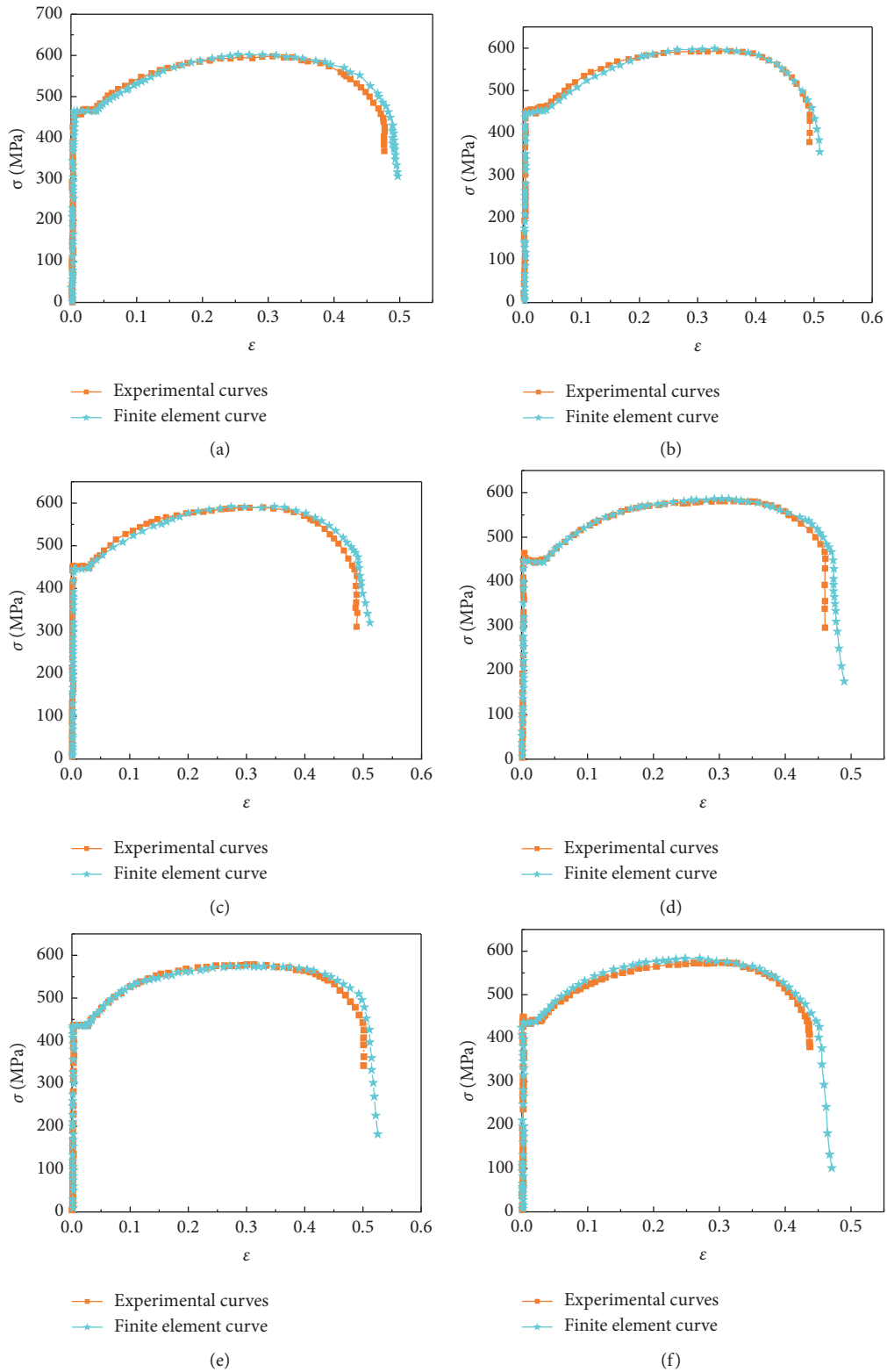FIGURE 17: Nominal stress-strain behavior of steel in tensile tests.

(a)

(b)

(c)
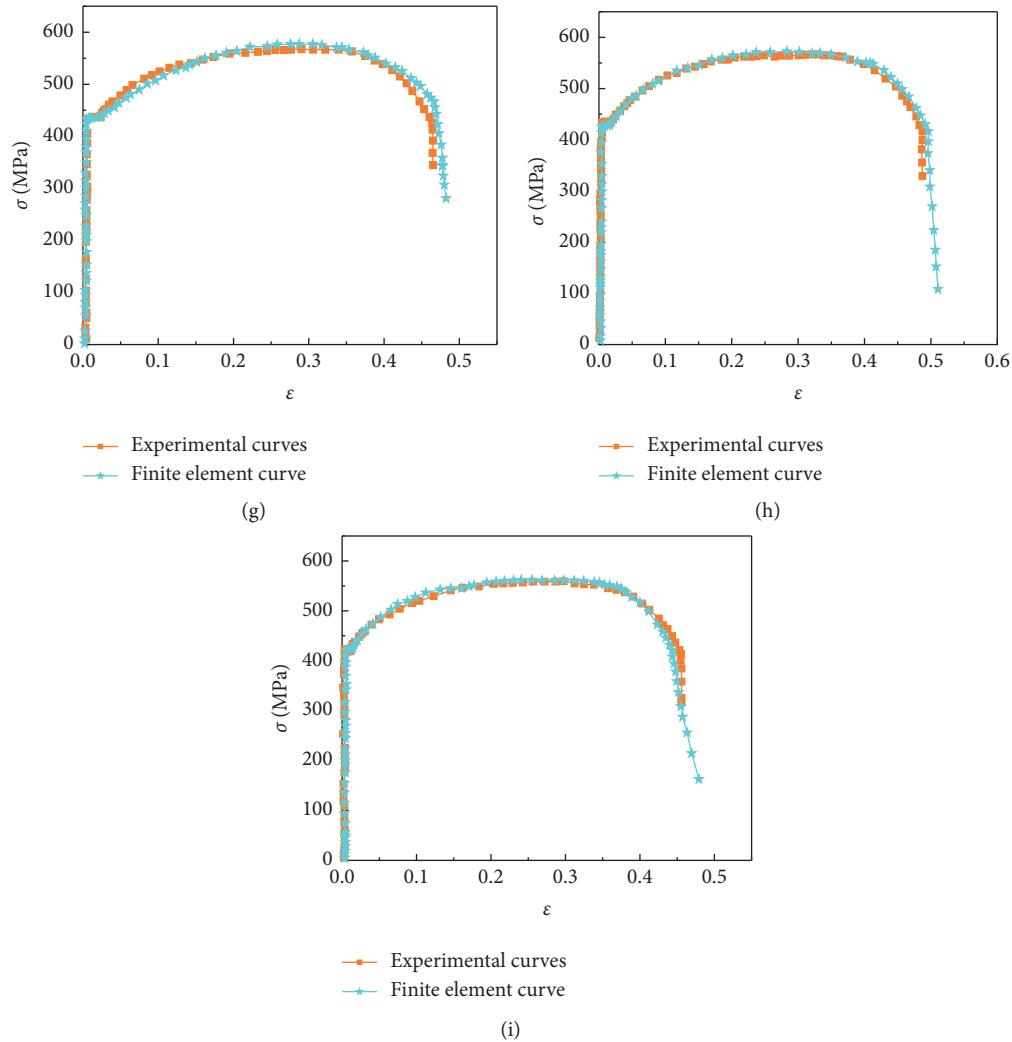
(d)

(e)

(f)

Figure 18: Continued.

(g)



(h)



(i)

FIGURE 18: Stress-strain curves of corroded Q345 steel. (a) 0 h, (b) 1 h, (c) 2 h, (d) 4 h, (e) 8 h, (f) 12 h, (g) 24 h, (h) 48 h, and (i) 72 h.

some deviations from experimental curves to some extent after necking. It is worth noting that errors are all within 5%. It can be proved that FEM can simulate the test in practice in light of stress-strain curves of strong acid-corroded steel Q345 between test and finite elements.

## 6. Conclusions

This study conducts a sequence of tests, FEM analyses, and theoretical research to propose a simplified model that properly investigates microscopic connections between surface morphology and mechanical degradation of steel Q345 under strong acid corrosion. The relevant results of the investigation concluded that

(1) The DSX500 noncontact topography scanner measured geometric parameters of corrosion pits on the surface of steel Q345. Due to the high concentration of hydrochloric acid during the early stage of corrosion, many pinhole-like corrosion pits exist on the surface of specimens along the vertical direction. Cone-shaped corrosion pits continue to appear in

steel with the extension of corrosion times. In the later stage of corrosion, the pits continued to expand, developing hemispherical and ellipsoidal shapes, so the adjacent pits were slowly connected.

(2) By observing fracture, steel represented different positions and shapes of the fracture. Most corrosion specimens fractured on the surface or on the bottom of pits rather than the center of pits. The size of pits on the surface of steel was inversely proportional to the size of dimples, revealing the fracture mechanism of steel from ductile failure to brittle failure.

(3) Compared with uncorroded specimens, it was found that corroded specimens represented that the nominal elastic modulus, nominal yield strength, nominal tensile strength, yield strength ratio, and elongation after fracture decreased by 19.55%, 10.37%, 6.60%, 4.03%, and 41.12%, respectively.

(4) Together with test results, mechanical degradation of corroded steel fit with the maximum pit impact factor and corrosion times. FEM based on uniform corrosion pits is found by flexible damage evolution

criterion. Its calculations match well with experimental results, indicating that this model can display the surface morphology of strong corrosion steel, and stress flow law and necking failure of strong corrosion steel accurately.

## Data Availability

The data used to support the findings of this study are available from the corresponding author upon request.

## Conflicts of Interest

The authors declare that they have no conflicts of interest.

## Acknowledgments

## References

[1] W. J. Qiao, H. Y. Zhu, and G. Zhang, "Mechanical properties and failure mechanism of steel plate composite beams under strong corrosion," *Journal of Chang'an University (Natural Science Edition)*, vol. 41, no. 2, pp. 46–54, 2021.

[2] R. Wang, R. Ajit Shenoi, and A. Sobey, "Ultimate strength assessment of plated steel structures with random pitting corrosion damage," *Journal of Constructional Steel Research*, vol. 143, pp. 331–342, 2018.

[3] J. M. R. S. Appuhamy, T. Kaita, M. Ohga, and K. Fujii, "Prediction of residual strength of corroded tensile steel plates," *International Journal of Steel Structures*, vol. 11, no. 1, pp. 65–79, 2011.

[4] A. Rahbar-Ranji, "Ultimate strength of corroded steel plates with irregular surfaces under in-plane compression," *Ocean Engineering*, vol. 54, pp. 261–269, 2012.

[5] F. Liao, W. Wang, and Y. Chen, "Ductile fracture prediction for welded steel connections under monotonic loading based on micromechanical fracture criteria," *Engineering Structures*, vol. 94, pp. 16–28, 2015.

[6] H. U. Sajid and R. Kiran, "Influence of corrosion and surface roughness on wettability of ASTM A36 steels," *Journal of Constructional Steel Research*, vol. 144, pp. 310–326, 2018.

[7] Z. Y. Jie, Y. D. Li, and X. Wei, "A study of fatigue crack growth from artificial corrosion pits at welded joints under complex stress fields," *Fatigue and Fracture of Engineering Materials and Structures*, vol. 40, no. 9, pp. 1364–1377, 2017.

[8] Y. Garbatov, C. Guedes Soares, J. Parunov, and J. Kodvanj, "Tensile strength assessment of corroded small scale specimens," *Corrosion Science*, vol. 85, pp. 296–303, 2014.

[9] I. Fernandez, K. Lundgren, and K. Zandi, "Evaluation of Corrosion Level of Naturally Corroded Bars Using Different Cleaning Methods, Computed Tomography, and 3D Optical Scanning," *Materials and Structures*, vol. 51, no. 3, p. 78, 2018.

[10] M. M. Kashani, A. J. Crewe, and N. A. Alexander, "Use of a 3D optical measurement technique for stochastic corrosion pattern analysis of reinforcing bars subjected to accelerated corrosion," *Corrosion Science*, vol. 73, pp. 208–221, 2013.

[11] B. Nie, S. Xu, J. Yu, and H. Zhang, "Experimental investigation of mechanical properties of corroded cold-formed steels," *Journal of Constructional Steel Research*, vol. 162, p. 105706, 2019.

[12] S. Bajracharya, E. Sasaki, and H. Tamura, "Numerical study on corrosion profile estimation of a corroded steel plate using eddy current," *Structure and Infrastructure Engineering*, vol. 15, no. 9, pp. 1151–1164, 2019.

[13] G.-C. Qin, S.-h. Xu, D.-q. Yao, and Z.-X. Zhang, "Study on the degradation of mechanical properties of corroded steel plates based on surface topography," *Journal of Constructional Steel Research*, vol. 125, pp. 205–217, 2016.

[14] S. Xu, H. Zhang, and Y. Wang, "Estimation of the properties of corroded steel plates exposed to salt-spray atmosphere," *Corrosion Engineering, Science and Technology*, vol. 54, no. 5, pp. 431–443, 2019.

[15] F. Caleyo, J. C. Velázquez, A. Valor, and J. M. Hallen, "Probability distribution of pitting corrosion depth and rate in underground pipelines: a Monte Carlo study," *Corrosion Science*, vol. 51, no. 9, pp. 1925–1934, 2009.

[16] S. B. Ren, Y. Gu, C. Kong, G. Song, X. Shanhua, and Y. Liqiong, "Effects of the corrosion pitting parameters on the mechanical properties of corroded steel," *Construction and Building Materials*, vol. 272, 2021.

[17] S. H. Xu, H. Zhang, B. Nie, and Z. Zhang, "Effect of pitting corrosion on the stress intensity factor magnitude and distribution," *International Journal of Steel Structures*, vol. 21, no. 4, pp. 1454–1464, 2021.

[18] R. M. Pidaparti and A. S. Rao, "Analysis of pits induced stresses due to metal corrosion," *Corrosion Science*, vol. 50, no. 7, pp. 1932–1938, 2008.

[19] J. Garcia-Manrique, D. Camas-Peña, J. Lopez-Martinez, and A. Gonzalez-Herrera, "Analysis of the stress intensity factor Along the thickness: the concept of pivot node on straight crack fronts," *Fatigue and Fracture of Engineering Materials and Structures*, vol. 41, no. 4, pp. 869–880, 2018.

[20] K. V. Rybalka, V. S. Shaldaev, L. A. Beketaeva, and A. N. A. D. Malofeeva, "Development of pitting corrosion of stainless steel 403 in sodium chloride solutions," *Russian Journal of Electrochemistry*, vol. 46, no. 2, pp. 196–204, 2010.

[21] H. Wang, S. Xu, Y. Wang, and A. Li, "Effect of pitting degradation on ductile fracture initiation of steel butt-welded joints," *Journal of Constructional Steel Research*, vol. 148, pp. 436–449, 2018a.

[22] M. M. Ahmmad and Y. Sumi, "Strength and deformability of corroded steel plates under quasi-static tensile load," *Journal of Marine Science and Technology*, vol. 15, no. 1, pp. 1–15, 2009.

[23] T. Gb, "Steel and Steel Products-Location and Preparation of Test Pieces for Mechanical Testing," 1998, https://www.saiglobal.com/PDFTemp/Previews/OSH/ISO/ISO_12345_05-01/T004356E.PDF.

[24] T. Gb, "High Strength Low Alloy Structural Steels," 2008, https://www.asminternational.org/documents/10192/3466171/06117_Chapter%203B.pdf/a764507a-3499-4d23-b348-5536d31c0ba2.

[25] T. Gb, "Metallic Materials-Tensile Testing-Part 1: Method of Test at Room Temperature," 2010, https://www.trl.com/iso_6892_1_tensile_testing_metallic_materials_at_room_temperature/.

[26] F. Yang, M. M. Yuan, W. J. Qiao, and N. N. B. Li, "Mechanical degradation of Q345 weathering steel and Q345 carbon steel under acid corrosion," *Advances in Materials Science and Engineering*, vol. 2022, Article ID 6764915, 19 pages, 2022.

[27] H. Zhang, S. Xu, Z. Zhang, and B. L. Nie, "Fracture analysis of corroded cold-formed thin steel plates based on actual morphology using micromechanical models," *Construction and Building Materials*, vol. 267, Article ID 120899, 2021.

[28] H. Zhang, S. Xu, B. Nie, and Y. Wen, "Effect of corrosion on the fracture properties of steel plates," *Construction and Building Materials*, vol. 225, pp. 1202–1213, 2019.

[29] Y. J. Shi, M. Wang, and Y. Q. Wang, "Experimental study on constitutive relationship of structural steel under cyclic loading," *Journal of Building Materials*, vol. 15, no. 3, pp. 293–300, 2012.

[30] H. L. Yu and D. Y. Jeong, "Application of a stress triaxiality dependent fracture criterion in the finite element analysis of unnotched charpy specimens," *Theoretical and Applied Fracture Mechanics*, vol. 54, no. 1, pp. 54–62, 2010.

[31] M. Cerit, "Numerical investigation on torsional stress concentration factor at the semi elliptical corrosion pit," *Corrosion Science*, vol. 67, pp. 225–232, 2013.